DOI:
10.1109/TBME.2009.2032164

Document Version
Peer reviewed version

Rolling Mechanical Imaging for Tissue Abnormality Localization during MIS

Hongbin Liu, David P. Noonan, Ben J. Challacombe, Prokar Dasgupta, Lakmal D. Seneviratne, *Member, IEEE* and Kaspar Althoefer, *Member, IEEE*

***Abstract*—We describe a novel approach for the localization of tissue abnormalities during minimally invasive surgery (MIS) using a force sensitive wheeled probe. The concept is to fuse the kinaesthetic information from the wheel-tissue rolling interaction into a pseudo-color rolling mechanical image (RMI) to visualize the spatial variation of stiffness within the internal tissue structure. Since tissue abnormalities are often firmer than the surrounding organ or parenchyma, a surgeon then can localize abnormalities by analyzing the image. Initially, a testing facility for validating the concept in an *ex vivo* setting was developed and used to investigate rolling "wheel-tissue" interaction. A silicone soft tissue phantom with embedded hard nodules was constructed to allow for experimental comparison between a RMI and a known soft tissue structure. Tests have also been performed on excised porcine organs to show the efficacy of the method when applied to biological soft tissues. Results indicate that the RMI technique is particularly suited to identifying the stiffness distribution within a tissue sample, as the continuous force measurement along a given rolling trajectory provides repeatable information regarding relative variations in the normal tissue response. When compared to multiple discrete uniaxial indentations, the continuous measurement approach of RMI is shown to be more sensitive and facilitates coverage of a large area in a short period of time. Furthermore, if parametric classification of tissue properties based on a uniaxial tissue indentation model is desirable, the rolling indentation probe can be easily employed as a uniaxial indenter.**

***Index Terms*— Soft tissue abnormality localization, haptics, minimally invasive surgery**

I. Introduction

THE world's first laparoscopic cholecystectomy in 1985 [1] represented the beginning of a surgical paradigm shift whereby certain procedures which were previously carried out using a single large incision would instead be performed in a minimally invasive manner through small incisions. Since then the technique of minimally invasive surgery (MIS) has been developed, been matured, and become increasingly popular in operating rooms worldwide. When compared with traditional "open" surgery, it has been shown that MIS offers many advantages including reduced tissue trauma, improved therapeutic outcome and earlier post operative recovery. However, these advantages come at the cost of an increase in the technical skills of the operating surgeon to perform MIS competently. Notable difficulties include the lack of direct visualisation of the operative site, reduced distal dexterity due to the use of long, rigid instruments introduced through a fixed point and the absence of direct tissue interaction. This reduction of visual feedback and the sense of touch, coupled with impaired dexterity can lead to accidental tissue damage [2]. In order to reduce the complexity of performing MIS, surgical robots have been developed. The system provides a complete surgical platform is the daVinci Surgical System™ from Intuitive Surgical. The daVinci is a master-slave tele-manipulator which separates the surgeons completely from the patient by placing them in an immersive stereoscopic environment which realigns the motor and visual co-ordinate systems, improves distal dexterity and facilitates intuitive control of seven degrees of freedom end-effectors. While the daVinci represents significant improvements over standard MIS, the sense of touch for a surgeon is quite limited.

This sense of touch, which is readily available during open surgery, provides the surgeon with valuable information regarding the potential extent of disease and margins of safety. The loss of such sensation could lead to a situation where a surgeon leaves a tumor (or part of a tumor) behind. During open procedures surgeons often avoid this by identifying the tumor and its boundaries by palpation and hence ensure that a negative margin is achieved when excising the cancer. In MIS, surgeons need to apply other techniques in order to identify a tumor's location and extent. It is possible to use imaging modalities such as magnetic resonance imaging (MRI) or computed tomography (CT) imaging to identify tumor locations pre-operatively. However, due to the deformability of soft tissue and likely movement of organs during the surgical procedure, it is very difficult to accurately register the pre-operative images to the intra-operative tumor locations. In robotic urological procedures the lack of the sense of touch can cause problems for identifying locally advanced T3 prostate cancer and large bulky muscle invasive bladder cancer. Thus, replicating the ability of palpating the tissue during robotics-assisted surgical procedures would be clinically beneficial.

The sense of "feel" by the human hand includes both force (kinaesthetic) sensing and tactile (cutaneous) sensing [3]. To

Manuscript received November 11, 2008.

H. liu, L. Seneviratne and K. Althoefer are with Kings College London, Division of Engineering, London, SW2R 2LS, UK (phone : 44-020-78481862; fax: 44-020-7848-2932; e-mail: hongbin.liu @ kcl.ac.uk; lakmal.Seneviratne@kcl.ac.uk; k.althoefer@kcl.ac.uk).

N. P. Noonan is with Imperial College London, Institute of Biomedical Engineering, London, South Kensington Campus, London, SW7 2AZ, UK (e-mail: dnoonan@imperial.ac.uk).

B. J. Challacombe is with Royal Melbourne Hospital, Department of Urology, Grattan Street Melbourne, VIC 3050, Australia (e-mail: benchallacombe@doctors.org.uk).

P. Gasgupta is with the Department of Urology, Guy's Hospital,St. Thomas' Street, London SE1 9RT, UK (email: prokarurol@gmail.com)

provide surgeons the substitute of palpation during MIS, researches have created smart instruments which are capable of acquiring partial haptic feedback, either force or tactile information [4]. In [5], a snake-like robot was developed to sense the applied force via analysis of its mechanism kinematics, allowing force sensing in environments where space or sterilization constraints do not permit the placement of standard force sensors. In [6, 7], computerized laparoscopic graspers with embedded strain gauges was developed to detect the compliance of the object through the measurement of grasping force with respect to grasper position. In [8], the feasibility of utilizing a force-sensitive probe to localize lung tumors based on variations in tissue stiffness is discussed. While force sensing is a promising approach for replacing palpation to identify tissue abnormalities during MIS, identifying tissue abnormalities using the aforementioned techniques is often conducted in a discrete manner e.g. localized indentation or tissue grasping. This can cause difficulties when attempting to identify tissue abnormalities through relative variations in tissue response, since a large tissue area may require investigation, and careful calibration must be carried out to account for changing boundary conditions. In order to allow a surgeon to rapidly investigate the tissue properties of a large area, tactile sensing arrays have been used to "mechanically image" the extended tissue regions [9, 10]. The use of a transrectal probe equipped with tactile sensors to identify prostate tumors has also been described [11]. Tactile feedback systems have also been proposed for locating pulmonary tumors [12], classifying breast lesions [13] and identifying arteries during robotic surgery [14]. In [15, 16], a tactile sensing instrument (TSI) has been developed to aid the surgeon in tumor localization during MIS. The TSI is equipped with a dense tactile sensor array at the instrument tip and can pass through a 10 mm trocar port. By successively palpating the tissue using the TSI, the distributed tactile image measured from multiple palpations can be combined into a panoramic view of the investigating tissue to visualize locations of the embedded tumors. Results from such research demonstrate that tactile feedback systems do provide more localized information than force sensing instruments and hence have potential as diagnostic tools. However, to cover a large tissue area and investigate relative variations over that area, such sensing arrays must either be very large or perform multiple discrete indentations [15, 16].

As such, the purpose of this paper is to introduce a new technique for tissue abnormalities localization during MIS. Our method employs a wheeled indenter equipped with a force/torque (F/T) sensor to perform continuous wheel-tissue rolling indentation along fixed trajectories. This technique is capable of covering large tissue areas in short time. By fusing the tissue reaction forces measured along trajectories, the variations in mechanical tissue properties can be mapped into a rolling mechanical image (RMI) which indicates the geometrical stiffness distribution of the examined tissue. Since the stiffness of a malignant tissue such as a tumor is typically higher than the surrounding healthy tissue [17, 18], a surgeon can exploit the color information provided by the RMI to distinguish abnormal tissue regions from healthy areas. As only a force/torque sensor and a positioning system are required, the miniaturization and adaptation of the wheel rolling indentation technique for robotic MIS is promising.

To characterize the soft tissue mechanical properties in further detail, uniaxial palpations can be applied at each of the abnormal regions as identified using the rolling imaging approach. From these uniaxial indentations the constitutive equation for each tissue region can be determined.

II. Rolling Indentation Technique

A. Force Sensitive Wheeled Probe

In order to evaluate rolling "wheel-tissue" interaction in a laboratory setting, a force sensitive wheeled probe, as shown in Fig.1 (a), was constructed. A cylindrical plastic wheel (diameter 8 mm, width 8 mm) was used as the end-effector. Twelve teeth were machined around the circumference of the wheel to avoid slip during rolling. The wheel is mounted on a ball bearing and is free to rotate about axis J_1. Two further axes of rotation, J_2 and J_3, are available; they can be either locked or unlocked to permit free rotation in all directions; when unlocked the wheel is capable of following curved trajectories in a three dimensional space. An offset of 2 mm between the center of the wheel and axis J_3 facilitates the probe wheel to adjust to a new trajectory during turning maneuvers — this behavior is attributed to the additional torque about J_3 generated by the offset. An ATI NANO17 Force/Torque sensor (SI-12-0.12 with a resolution of 0.003 N and interfaced to a computer via a 16-bit DAQ (National Instruments PCI 6034E)) is connected to the wheeled probe via an interface plate. This allows for the measurement of the three force components (F_x, F_y, F_z) imparted by the tissue onto the probe wheel as it is rolling over the tissue surface.

In order to prescribe a desired trajectory over the surface of a soft tissue sample (usually keeping the indentation depth constant), the unit (wheeled probe and F/T sensor) is attached to the distal tip of a Mitsubishi RV-6SL 6-DoF manipulator.

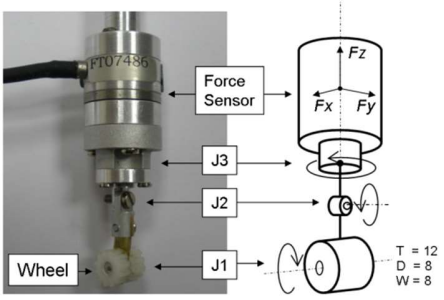

Fig. 1. The force-sensitive probe with a grooved wheel end-effector; The wheel has 12 teeth (T) along its circumference, is 8 mm in diameter (D) and 8 mm in width (W).

B. Rolling Indentation Dynamics

Before converting the force signals measured from the F/T sensor (F_x, F_y, F_z) into a RMI, a preliminary analysis of the rolling indentation dynamics was conducted to determine which force component(s) should be utilized to generate an accurate representation of the force applied by the tissue onto the wheel. In [19] a model of the interaction between a wheel and underlying soft tissue is presented. In this case, the soft tissue is represented using a Voight model (spring and dashpot in parallel) covered by a membrane in tension. The resultant

(vertical) force imparted by the tissue onto the wheel is a function of the pressure due to tissue deformation, the vertical component of the membrane tension and the vertical component of the shear force between the wheel and the tissue. However, the parameters required to populate this model include the viscosity of the peritoneal fluid (to calculate the shear force component) and simultaneous fore and aft wheel contact angles (to calculate membrane tension component) — all of which are difficult to measure.

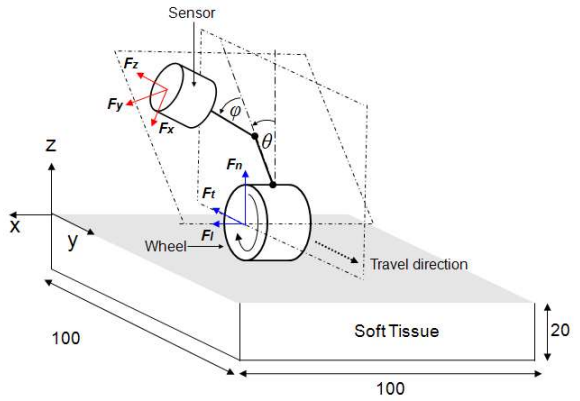

Fig.2. Schematic of rolling indentation showing the relationship between F_x, F_y, F_z and F_l, F_t, F_n; all dimensions are in "mm".

For generating a RMI, the rolling dynamics are simplified and it is assumed that the force applied by the tissue onto the wheel (rolling force) can be abbreviated as only consisting of the normal force (perpendicular to the travel direction of the wheel), the tangential force (parallel to the wheel travel direction) and the lateral force (along the axis of wheel rotation). These forces are illustrated in Fig. 2, where F_n is the normal force, F_t is the tangential force, and F_l is the lateral force. Also shown in Fig. 2 are the force components F_x, F_y, F_z measured by the multi-axial F/T sensor. For a perfectly flat tissue surface, it can be assumed that the measured forces F_x, F_y, F_z map directly to F_l, F_t, F_n. However, in practice the surface of soft tissue is uneven with variations in both pitch, θ, and roll, φ. In order to investigate the effect of this uneven surface on the rolling dynamics, the angles of pitch, θ, and roll, φ, are introduced in Fig. 2. Thus, if, θ and φ are known, forces F_l, F_t, F_n can be calculated using F_x, F_y, F_z:

$$\begin{bmatrix} F_l \\ F_t \\ F_n \end{bmatrix} = \begin{bmatrix} \cos\varphi & -\sin\theta\sin\varphi & \sin\varphi\cos\theta \\ 0 & \cos\theta & \sin\theta \\ -\sin\varphi & -\sin\theta\cos\varphi & \cos\theta\cos\varphi \end{bmatrix}^{-1} \begin{bmatrix} F_x \\ F_y \\ F_z \end{bmatrix} \quad (1)$$

Based on the assumption that the information contained in F_n is primarily due to the compression of the soft tissue (rather than the shear force and membrane force), measuring the variations in F_n as the probe traverses the tissue is suitable for generating the RMI (from $F_n = F_z$). However, as indicated above, for an uneven surface the measured value of F_z will change depending on the surface topology. To ensure that the F/T sensor is measuring the correct value of F_n would require calculating the angles of θ and φ with respect to F_z and adjusting the orientation of the end-effector in such a way that F_z and F_n are always in the same plane. However, this would significantly increase the complexity of the system and, thus, an alternative solution is proposed. In order to investigate the effect of changing the roll angle, θ, and pitch angle, φ, on the relationship between F_n, F_t and F_l, two sets of rolling indentation experiments were conducted on a flat homogenous silicone block with the dimensions of 100 ×100 × 20 mm^3. The used silicone block was made of the RTV6166 gel (General Electric) which has mechanical behaviors similar to biological soft tissues [20]. During the first test the roll angle, θ, was kept at 0° and the pitch angle, φ, was increased from 0° to 60° in 5° increments. The manipulator was programmed to follow ten trajectories parallel to the *y-axis* as shown in Fig. 2 at a speed of 15 mm/s. Each trajectory was 80 mm in length; the probe was shifted by 8 mm along the *x-axis* at the end of each trajectory and then a new trajectory parallel to the previous one was carried out. The wheel was rolled across the silicone block at indentation depths ranging from 2 mm to 4.5 mm and incrementing the indentation depth by 0.5 mm. This procedure was repeated 12 times for each pitch angle. The second test followed the same procedure except that the pitch angle, φ, was kept at 0° and the roll angle, θ, was increased from 0° to 60° in 5° increments. Forces F_t, F_n and F_l were then determined using the F/T sensor readings and Eq.1. It was found that during both tests, the lateral force $F_l \approx 0$, as virtually no lateral motion occurred during the rolling indentation. However, as can be seen in Fig. 3, the ratio F_t/F_n remains almost constant regardless the change of θ and φ (mean ratio F_t/F_n =0.084, Standard Deviation = 0.008). This indicates that even when changing the surface topology, the normal force dominates the force signal.

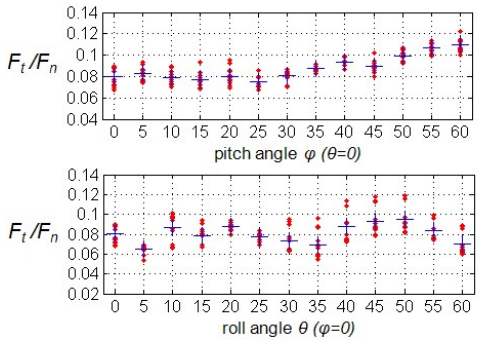

Fig.3. F_t/F_n ratio with different roll angle and pitch angle during rolling indentation; dots are the values of each test, crosshairs indicate the average value for each roll angle and pitch angle.

The acquired data can be also used to analyze the resultant force, F_r, which is a function of F_l and F_t :

$$F_r = \sqrt{F_n^2 + F_t^2 + F_l^2} = \sqrt{F_x^2 + F_y^2 + F_z^2}$$

The data acquired from both experiments ($\theta = 0$ and $\varphi = 0$) can be used to show that the relationship between the measured resultant force, F_r, and the ground truth normal force, F_n (calculated using Eq. 1 for all values of θ and φ), is: $F_r \approx F_n$. By analyzing the experimental data, it is found that the ratio of F_n/F_r approaches 1 (average F_n/F_r =0.99), and the ratio F_t/F_r approaches 0 (average F_t/F_r =0.08), regardless of the values of θ and φ. The above shows that even for an uneven surface it is possible to accurately measure F_n without measuring or changing the orientation of the end-effector; instead the multi-axis sensing capability of the F/T sensor is

sufficient to determine F_r, since $F_r \approx F_n$. It is, thus, possible to use the resultant force F_r to generate the RMI.

C. Generating a Rolling Mechanical Image

To generate the RMIs presented in this paper, a series of trajectories were defined to cover the surface of each test sample. The wheeled probe then traveled along each trajectory with a constant indentation depth and speed. The force imparted by the soft tissue, as measured by the F/T sensor, was recorded during each traverse at a sampling rate of 100 Hz. To generate a RMI, the resultant forces, F_r (of the force components F_x, F_y and F_z as acquired by the F/T sensor), at each sampled location along each trajectory were fused together to form a pseudo–color RMI. The RMI projects the geometry of the stiffness distribution over the test area onto the *x-y* plane and the stiffness variation is represented using a pseudo color scheme. When analyzing the images a color code indicates the stiffness — with red representing the highest stiffness value and blue the lowest. Further analysis can be performed by converting the RMI into a force contour map using the *Matlab*^{TM}. In this representation, the *(x, y)* location of the centroid of stiff regions can be readily identified using the apexes on the contour map. This gives an *(x, y)* coordinate of the centroid of a stiff region and can be used to compare the results from the RMI to the known ground truth location of an embedded nodule. This approach is employed in Section III.

D. Uniaxial Palpation

The information provided within the RMIs can be used to identify the location of underlying tissue abnormalities. To further identify the viscoelastic properties of these abnormal regions, additional uniaxial palpation tests can be applied in conjunction with parametric modeling. A unique feature of the force sensitive wheeled probe is that one can easily switch between rolling indentation and uniaxial indentation when and where required. In Quasi-Linear Viscoelasticity theory (QLV) [27], the stress developed in a specimen is considered a function of stretch λ as well as time t. If a soft tissue sample is subjected to a monotonic stretch from 0 to λ in a time interval ζ, the constitutive equation of the tissue can be expressed as:

$$E(\lambda,t) = E^{(e)}(\lambda) + \int_0^{\zeta} E^{(e)}[\lambda(\varsigma - t)]\frac{\partial G(t)}{\partial t}dt, \quad (2)$$

where $E^{(e)}(\lambda)$ is the elastic response — an instantaneous stress generated when a step function with a stretch ratio λ is imposed on the sample. $G(t)$ is the reduced relaxation function and is a normalized function of time. Let the compressive stretch $\lambda = L / L_0$, and the compressive strain $\varepsilon = (L_0 - L) / L_0 = 1-\lambda$, then the elastic response $E^{(e)}(\lambda)$ can be defined as:

$$E^{(e)}(\lambda) = \alpha(e^{\beta(1-\lambda)} - 1), \quad (3)$$

where α and β are unknown constant parameters, L_0 is the thickness of the tissue at zero loading, and L is the thickness of the tissue when compressed by the load. The reduced relaxation function can be modeled by a sum of exponential functions [21]. In our previous work, it was shown that using a sum of two exponentials can accurately model the stress relaxation curve [22], thus

$$G(t) = \frac{C_1 e^{-V_1 t} + C_2 e^{-V_2 t}}{C_1 + C_2}. \quad (4)$$

As indicated in Eq. 2, function $E^{(e)}(\lambda)$ and $G(t)$ need to be identified in order to obtain the constitutive equation of tissue. This was achieved through carefully designed uniaxial palpation. The palpation test followed a two phase protocol:

First, the wheel was indented vertically into the desired region on the silicone phantom to a specific depth with a constant speed. As the $E^{(e)}(\lambda)$ can be approximated by the stress response when applying a ramp strain function input with a sufficiently high loading rate [21]. Thus, the stress-strain function obtained from the vertical indentation can be considered a good approximation of the $E^{(e)}(\lambda)$.

Second, after the vertical indentation, the probe was held at the same indentation depth for a fixed period. This procedure is designed to obtain the reduced relaxation function $G(t)$ from the stress relaxation curve.

E. Testing Materials

To evaluate the proposed rolling mechanical imaging technique for identifying relative variations in tissue stiffness, experiments have been conducted on a silicone soft tissue phantom as well as samples of porcine kidneys. The silicone phantom was constructed using RTV6166 gel with nine rubber nodules (simulated areas of high stiffness) embedded at various depths. The dimensions of the phantom and the location of each embedded nodule are shown in Fig.4. The properties of shape, thickness and depth under the surface of each nodule are listed in Table I. In addition, the elastic moduli of the rubber nodule and the silicone are 21.9×10^4Pa and 14.7×10^3 Pa, respectively. To investigate the efficacy of rolling mechanical imaging on biological soft tissue, *ex vivo* experiments have also been conducted on two porcine kidney samples K_1 and K_2 (weight =0.24 kg and 0.2kg, lab temperature = 12.1°C, lab humidity = 30%). To further examine the ability of the technique to identify an abnormality based on changes in the stiffness distribution; two simulated tumors (T_1 and T_2) were constructed using the same silicone gel as before and were respectively embedded within the kidneys, as shown in Fig. 5(a). The dimensions and shapes of T_1 and T_2 are shown in Fig.5 (b). From experimental tests, the elastic moduli of the kidney samples were found to be 18.6×10^3 Pa and 20.6×10^3 Pa, and the elastic modulus of both T_1 and T_2 is 54.2×10^3 Pa.

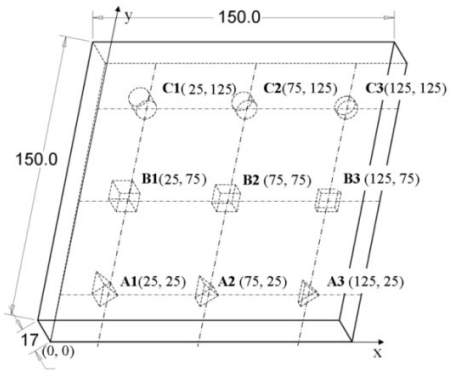

Fig. 4. The dimension of the silicone soft tissue phantom displaying location, shape and depth of the nine embedded rubber nodules (A1, A2, A3 have a triangular cross section, B1, B2 and B3 have a square cross section, C1, C2, C3 have a circular cross section). All dimensions are in "mm".

TABLE I
DIMENSIONS AND LOCATIONS OF NODULES EMBEDDED WITHIN THE SILICONE PHANTOM (ALL DIMENSIONS ARE IN "MM")

Nodules	Cross section	Thickness	Depth	Location (x, y)
A1		12	5	25, 25
A2		8	7	75, 25
A3		4	13	125, 25
B1		12	5	25, 75
B2		8	7	75, 75
B3		4	13	125, 75
C1		12	5	25, 125
C2		8	7	75, 125
C3		4	13	125,125

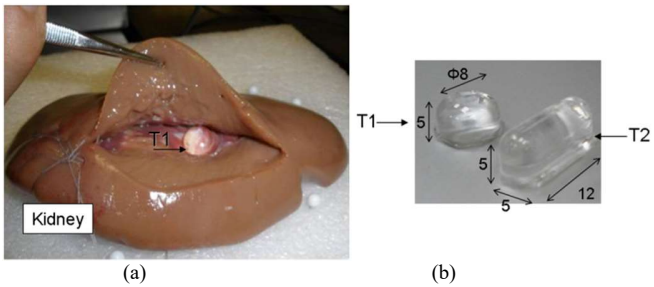

(a) (b)

Fig. 5(a). The nodules embedded within a porcine kidney sample. Fig. 6(b) The dimension of the simulated tumors T_1 and T_2.

III. EXPERIMENTAL RESULTS

A. Silicone Soft Tissue Phantom

1) Experimental Protocol

To examine the efficacy of abnormality localization using the rolling mechanical imaging technique, initial experiments were conducted on a silicone phantom containing embedded hard nodules (see Fig. 4). Using such a phantom allowed for a comparison between the image generated via rolling indentation and the known (ground truth) internal tissue structure. The protocol utilized for these tests is listed below:

First, a series of 36 trajectories parallel to the x-axis were defined, with a shift of 4 mm along the y-axis between each path. Each trajectory was 150 mm in length and the first trajectory started at (0, 0) position on the silicone phantom. An area of 150×144 mm^2 was covered during the experiment.

Second, the manipulator was programmed to traverse the wheeled probe along the predefined trajectories with a constant rolling indentation depth (initially 2 mm) at a speed of 45 mm/s. It took approximately 2 minutes and 30 seconds to cover the entire area. The force imparted by the silicone was recorded during each traverse at a sampling rate of 100 Hz. The rolling indentation depth was increased from 2 mm to 4 mm in 0.5 mm increments from one test to the next.

To thoroughly evaluate the repeatability and robustness of the abnormality localization, above procedures were repeated ten times for each indentation depth.

2) Data Analysis: Rolling Mechanical Imaging

After completion of the experiments, the RMIs were generated as described in Sections III. The embedded nodules are stiffer than the surrounding silicone. Hence their locations on the RMIs show up as high stiffness regions (red color). A RMI generated with 4 mm rolling indentation depth is shown in Fig. 6 (left). To analyze the efficacy of nodule localization, the RMI can be converted into force contour maps. The visible locations of apexes of the high stiffness regions (i.e. the *x, y* coordinates of the centroid of a nodule) were identified on the contour maps and are marked (by crosshairs), Fig.6 (right).

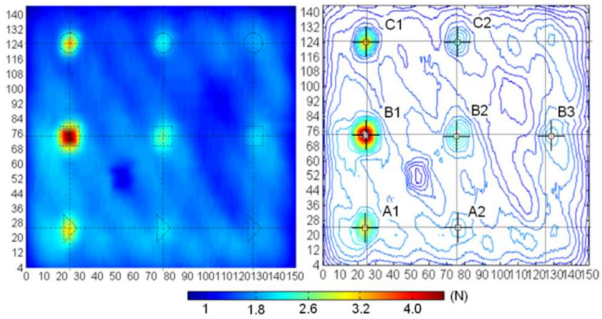

Fig. 6. The RMI (left) and the force contour map (right) for 4 mm rolling indentation depth on the silicone phantom; crosshairs on the contour map indicate the locations of each visible nodule.

To illustrate the repeatability of the technique each test was repeated ten times at each indentation depth, the locations of the identified nodules from repeated tests for each indentation depth are shown in Fig. 7. The averaged *(x, y)* locations of the identified nodules at each rolling indentation depth were compared to the corresponding ground truth *(x, y)* nodule locations. Table II shows the localization errors in *mm* for each identifiable nodule with respect to the known ground truth location. Table III lists the standard deviation results. Several observations can be made from Tables II and III. First, the number of embedded nodules visible in the images increases as the rolling indentation depth increases. Second, the identified locations of the visible nodules are accurate; compared to the ground truths, the errors of the identified nodule locations range from 0.20 mm to 1.42 mm in the *x-axis* and from 0.07 mm to 1.76 mm in the *y-axis*. Third, the rolling imaging technique is repeatable over multiple tests. The standard deviations of the identified nodule locations from ten repeated tests range from 0.58 mm to 1.89 mm in the *x-axis* and from 0.02 mm to 1.90 mm in the *y-axis*. Moreover, while the reaction forces from the embedded nodules increase with increasing indentation depth, the accuracy and repeatability of the identified nodule locations has no significant correlation with the rolling indentation depth. To further investigate the effect of rolling speed on the accuracy and repeatability of the rolling imaging method, the rolling tests with a indentation depth of 4 mm were conducted at a speed of 15 mm/s, 30 mm/s, 45 mm/s and 60 mm/s. For each speed, the test was repeated ten times. Localization errors, i.e. deviation from the ground truth, and the standard deviation of the localization errors were computed. The localization error of RMI method, e_l, is defined in the following form, $e_l = \sqrt{{e_x}^2 + {e_y}^2}$, where e_x and e_y are the coordinate errors of identified nodule locations in *x-axis* and *y-axis* respectively. The standard deviation of the localization errors, s_l, is defined as $s_l = \sqrt{{s_x}^2 + {s_y}^2}$, where s_x and s_y are the standard deviations of e_x and e_y respectively. Table IV shows the means of the e_l errors for each visible nodule, $\bar{e}_l$, at different rolling speeds, and the corresponding

standard deviation s_l. To further investigate the relationship between the location errors and the rolling speed, a null hypothesis test was conducted. It shows that the correlation coefficient c_r between error e_l and rolling speed is 0.009, and the corresponding p-value is 0.969. This indicates that error e_l has no significant correlation with the rolling speed (the correlation coefficient c_r is a number from -1 to 1, (c_r = ±1) indicates a perfect linear correlation, (c_r = 0) indicates no correlation; the p-value is a number from 0 to 1, when p-value is small (< 0.05), the correlation is significant). Moreover, the correlation coefficient c_r between s_l and rolling speed is -0.177, and the p-value is 0.366. This demonstrates that the correlation between s_l and rolling speed is not significant either. Hence, the accuracy and repeatability of this RMI technique are insensitive to changes in rolling speed.

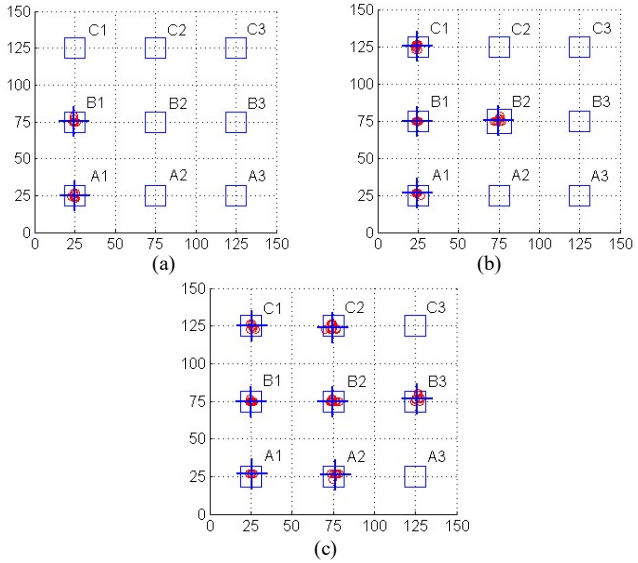

Fig. 7 The locations (x, y) of the identified nodules from 10 repeated tests for 2 mm (a), 3 mm (b) and 4 mm rolling indentation depth (c); circles on the map are the locations of each test, crosshairs indicate the average apex locations determined from the repeated tests. Where it was not able to identify a nodule, only the ground truth nodule location is shown using a square.

TABLE II
THE ERROR IN X,Y COORDINATES OF THE LOCALIZED NODULE FROM RMIS WITH ROLLING INDENTATION DEPTH (RD) FROM 2 TO 4 MM , NI=NOT IDENTIFIABLE, ALL DIMENSIONS ARE IN "MM"

	R_d=2.0	R_d=2.5	R_d=3.0	R_d=3.5	R_d=4.0
A1	0.28, 0.32	0.76, -0.92	0.56, -1.28	-0.77, -1.51	-0.65, -1.56
A2	NI	NI	NI	-1.21, -1.55	-1.42, -1.18
A3	NI	NI	NI	NI	NI
B1	0.40, -0.6	0.40, -0.40	0.25, 0.3	-0.30, -0.20	-0.20, 0.20
B2	NI	NI	0.17, -0.32	0.40, 0.43	0.34, 0.24
B3	NI	NI	NI	1.31, 1.24	-1.30, -1.76
C1	NI	1.31, 1.24	0.76, -0.28	-0.36, -0.15	-0.80, 0.04
C2	NI	NI	NI	-0.95, 0.07	0.50, 1.14
C3	NI	NI	NI	NI	NI

TABLE III
THE STANDARD DEVIATION OF X,Y COORDINATES OF THE LOCALIZED NODULE FROM RMIS FROM 2 TO 4 MM ROLLING INDENTATION DEPTH (RD), NI=NOT IDENTIFIABLE, ALL DIMENSIONS ARE IN "MM"

	R_d=2.0	R_d=2.5	R_d=3.0	R_d=3.5	R_d=4.0
A1	0.82, 1.74	0.67, 1.30	1.09, 0.54	0.71, 0.12	0.84, 0.02
A2	NI	NI	NI	1.89, 0.03	1.48, 1.20
A3	NI	NI	NI	NI	NI
B1	0.58, 1.40	0.79, 1.34	0.76, 0.27	0.93, 1.39	1.00, 0.63
B2	NI	NI	1.57, 1.39	1.00, 0.06	1.74, 0.84
B3	NI	NI	NI	1.07, 1.68	1.41, 1.88
C1	NI	1.08, 1.68	0.78, 1.67	1.45, 1.64	0.90, 0.49
C2	NI	NI	NI	1.83, 1.90	1.67, 1.86
C3	NI	NI	NI	NI	NI

TABLE IV
THE MEAN OF LOCATION ERRORS ($\bar{e}_l$) OF RMIS GENERATED AT DIFFERENT ROLLING SPEEDS (RSP) AND THE CORRESPONDING STANDARD DEVIATION OF LOCATION ERRORS (SL); THE ROLLING INDENTATION DEPTH IN ALL CASES IS 4 MM; SPEED UNITS ARE IN "MM/S", UNITS OF $\bar{e}_l$ AND SL ARE IN "MM".

Nodules		RSp=15	RSp=30	RSp=45	RSp=60
A1	$\bar{e}_l$	1.57	1.74	1.69	1.86
	s_l	0.71	0.70	0.84	0.86
A2	$\bar{e}_l$	1.35	1.68	1.84	1.35
	s_l	1.37	0.76	1.91	1.35
B1	$\bar{e}_l$	0.96	0.48	0.29	0.77
	s_l	0.95	1.13	1.18	0.80
B2	$\bar{e}_l$	0.83	0.51	0.42	1.00
	s_l	1.06	1.17	1.93	1.26
B3	$\bar{e}_l$	1.38	1.87	2.18	1.62
	s_l	1.76	1.51	1.65	1.89
C1	$\bar{e}_l$	1.92	1.70	0.80	1.78
	s_l	0.63	0.74	1.02	1.34
C2	$\bar{e}_l$	1.69	1.94	1.24	1.69
	s_l	2.09	2.12	1.99	2.13

Soft tissues can be preconditioned under successive loadings [21], i.e. the tissue stiffness (stress-strain curve) keeps decreasing until it reaches a steady condition. To investigate the effect of tissue preconditioning on the RMIs, the force signals of successive repeated rolling indention tests were analyzed. It was found that the preconditioning of tissue indeed affected the wheel-tissue interaction force signal, Fig.8. However, the variation of the force signal does not distort the accuracy and repeatability of the abnormality localization as they are determined by examining the relevant spatial change of force signal rather than the absolute force value, Fig.8. These results indicate that the RMI technique is capable of detecting changes in the stiffness of tissue and that when stiff areas are located, the technique is repeatable over multiple tests. However, the technique is not capable of identifying all embedded nodules which suggests that a sensitivity threshold does exist. This threshold is a function of the nodule size, relative variation in nodule stiffness when compared with the surrounding tissue, the depth that the nodule is buried beneath the surface and the rolling indentation depth. It is also necessary to mention that the changing of the wheel dimensions and surface profile resulted in a change in sensitivity and force range. However, a more in-depth evaluation of these effects is to be carried out for future work.

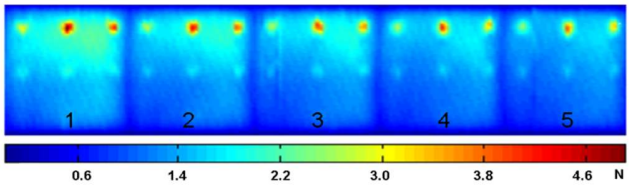

Fig.8. RMIs generated from five successive rolling indentations with an indentation depth of 4 mm and a rolling speed of 45 mm/s.

3) Data Analysis: Uniaxial Palpation

The RMIs generated indicate the location of embedded nodules. To further identify the viscoelastic properties of these abnormal tissue regions, additional uniaxial palpation can be

applied following the procedures below:

First, the wheel was indented vertically into the selected regions within the silicone phantom by a speed of 5 mm/s to a depth of 5 mm. The elastic response, $E^{(e)}(\lambda)$, of the tissue was identified by fitting a curve to the stress-strain representation of the tissue based on Eq.3; the nonlinear least square method was employed to minimize the error between fitted curve and the stress-strain function. R-square errors between 0.9929 and 0.9994 were achieved.

Second, when the wheel reached at a depth of 5 mm, it was kept constant at that depth for 5 seconds. The relaxation function G(t) was identified by fitting a curve to a representation of Eq.4. A nonlinear least square method was employed to minimize the error. The resultant R-square errors are between 0.9889 and 0.9964.

Fig.9 shows the selected locations at which uniaxial palpations were carried out and the corresponding stress-time curves obtained during these uniaxial palpations. The identified parameters of the QVL model for each test location are listed in Table V. It can be seen that the QVL model can accurately model the stress-time function of the silicone.

TABLE V
THE PARAMETERS OF TISSUE CONSTITUTIVE EQUATION OBTAINED FROM DIFFERENT TEST AREAS

	$\alpha \times 10^4$	β	C_1	C_2	V_1	V_2
A1	1.195	11.435	0.067	0.932	0.898	0.012
B1	0.553	16.291	0.062	0.937	0.861	0.012
C1	0.634	15.182	0.053	0.946	0.935	0.013
A2	0.956	10.366	0.050	0.949	1.115	0.009
B2	0.555	12.818	0.089	0.910	1.146	0.013
C2	0.818	10.819	0.096	0.903	1.014	0.014
B3	0.528	11.714	0.080	0.919	0.991	0.011
H1	0.873	9.611	0.081	0.918	1.005	0.012
H2	0.528	12.518	0.086	0.913	1.018	0.011

It is also seen that when analyzing the stress-time curves it is not easy to distinguish between two of the embedded nodules (B_2 and B_3) and two "nodule-free" silicon regions (H_1 and H_2) from analyzing the acquired stress-time curves. The reason is that locations, B_2, B_3, H_1 and H_2, have different boundary conditions and test boundary conditions have significant effect on the stress-time curves. Thus, it is difficult to distinguish the nodule containing and nodule-free region by only comparing their stress-time curves without taking into account the corresponding test boundary conditions. Conversely, B_2 and B_3 can be readily identified using the RMI approach. The reason RMI is superior to the stress-time curves in differentiating the embedded nodules is that, the stress-time curve only consists of the stress information at one single location while RMI contains the information of not only the specific nodule locations but also the surrounding nodule-free areas. Compare to the nodule location, the surrounding nodule-free areas have similar boundary conditions. Hence a minute relative difference in stiffness between a location with increased stiffness due to a buried nodule and nodule-free vicinity can be detected. Similar detection capabilities are expected when attempting to detect tumors inside otherwise healthy organs using the RMI approach. Manual palpation has shown to provide similar results: surgeons mainly rely on the feel of subtle relative change in tissue stiffness between the tumor and surrounding tissue and usually are not able to identify the absolute stiffness value of a tumor.

If the stress-time information were acquired from all locations of the test area, then the unison of all these curves will provide similar information regarding nodule locations as would the rolling indentation technique. However producing stress-time information for all locations is impractical because of the extraordinary time required. In contrast, rolling imaging can cover an entire tissue surface in a relatively short time and hence it is more efficient in nodule localization.

This demonstrates a key advantage of the RMI technique over the discrete uniaxial palpation approach. Namely, the continuous measurement of the tissue response from the rolling wheel can clearly and quickly identify subtle relative changes in the tissue mechanical response and obviates the necessity of performing numerous discrete indentations in order to obtain useful information regarding the stiffness distribution.

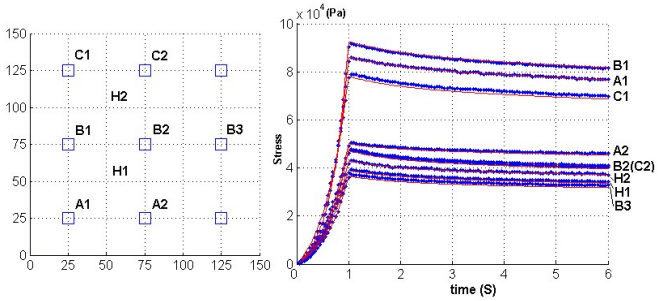

Fig. 9. The locations (x, y) of uniaxial palpation areas on the silicone phantom and the corresponding stress-time curves. The blue dots are the experimental data; the red solid lines are the simulation data from the QLV model.

B. Experiments on Excised Porcine Tissue

1) Experimental Protocol

While silicone phantom tests are useful for preliminary characterization, it is necessary to perform tests with biological soft tissue in an *ex vivo* setting to investigate the efficacy of the rolling mechanical imaging modality before moving towards *in vivo* experiments. One of the primary differences between the silicone soft tissue phantom and a biological soft tissue is the uneven, slick surface of natural organs. This presents difficulties in maintaining a constant indentation depth, avoiding wheel slip and accurately measuring the normal force response. In this paper, a preliminary *ex vivo* investigation on porcine kidneys is presented. To maintain a constant indentation depth on an uneven surface, a surface registration was conducted pre-experimentally on each sample by setting multiple waypoints on the surface of the tissue, as shown in Fig.10. At each waypoint the height of the tissue surface was visually determined by advancing the robot manipulator along the *z-axis* until wheel-tissue contact occurred. During the surface registration, a plastic cling film of negligible thickness was used to cover the entire sample to prevent loss of water content and thus tissue desiccation. To demonstrate the ability of the technique to identify the location of an embedded

nodule within a tissue sample, two kidneys (K_1 and K_2) were embedded with the simulated tumors described in Section 4. The simulated tumors T_1 and T_2 were buried separately into K_1, at a depth of 8 mm and then K_2 at a depth of 20 mm. The embedding was performed before surface registration and their locations in *x-y* plane were marked using pins. After the surface registration of each kidney, the locations of the simulated tumors were registered by touching the wheeled probe to the pins and recording the respective positions. The wheeled probe was then rolled across the kidney via the waypoints keeping the indentation depth as constant as possible, at a speed of 45 mm/s, to cover a 60×30 mm^2 area. An indentation depth of 3 mm was selected and the procedure was repeated three times on each kidney.

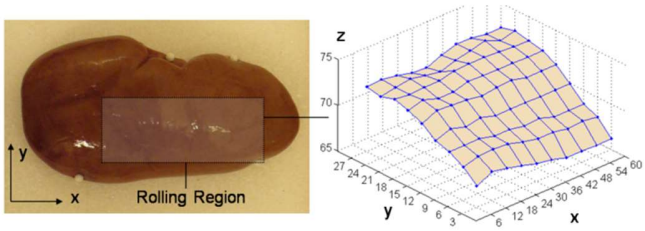

Fig.10. The surface registration of a porcine kidney by setting 90 waypoints in the test area. (a) The set up of *ex vivo* experiments where 4 pins were used to stabilize the sample on a Styrofoam sheet; (b) the surface map with solid dots indicating the predefined waypoints.

2) Data Analysis: Rolling Mechanical Imaging

It was found that when T_1 and T_2 were embedded into kidney K_1 at a depth of 8 mm, they could both be identified within the RMI. Fig. 11 shows the actual locations of T_1 and T_2 (marked by a circle) as well as the locations of the T_1 and T_2 identified from the force contour map for each of the three tests (marked by a cross). It is seen that the identified locations of T_1 and T_2 are in good agreement with their registered locations within the kidney (the averaged localization error in *mm* in the *x-y* plane for T_1 is (0.28, 0.52), for T_2 is (0.35, 0.95)) and this tumor localization is repeatable. The standard deviation in *mm* for T_1 is (0.53, 0.84), the standard deviation for T_2 is (0.38, 0.43). When T_1 and T_2 were embedded 20 mm deep into kidney K_2, the RMI was not capable of explicitly visualizing the two tumor substitutes. Although T_1 was not detectable using RMI, T_2 can be discovered by varying the image threshold, Fig. 12, despite the presence of the renal pelvis within the kidney dominates the image. To identify T_2 in the RMI, an image threshold was applied on the RMI (for every image pixel, if its value is above the threshold, the value of this pixel is set to be equal to the threshold). When the threshold value is set to 0.9 N, T_2 appears as a distinctive area in the image, Fig. 12. If the approximate size of the nodule is known from pre-operative images, a surgeon can confidently differentiate the nodule from the nodule-free area as well as the renal pelvis area in the RMI. It is noted that the regions by the RMI appear different from the shape of the embedded nodules. The authors have identified two reasons that may be attributed to the considerable change of shape in an object image when compared to the original object shape.

First, the finite width of the wheel introduces a localization error along the *y-axis*. The wheel has a width of 8 mm, and the rolling paths are parallel to the *x-axis*, with a 4 mm shift along the *y-axis*. Hence, the image resolution and accuracy in the direction of the *y-axis* will be limited by the wheel width.

Second, tissue deformation during rolling indentation introduces localization errors. As the kidney is an inhomogeneous soft tissue, as the wheel indents and rolls across the tissue it causes a slight "deformation wave" which propagates ahead of the wheel. When the wheel rolls along different rolling paths, this "deformation wave" may not identical. This can potentially cause a small misalignment on the RMIs. This phenomenon occurred more often at high speed rolling indentations than low speed indentations. However, from all the *ex vivo* experiments conducted so far, such misalignment has not caused sufficient distortion to affect the accuracy of the abnormality localization. As indicated in Table IV, experimental results show that the accuracy and repeatability of this technique are insensitive to changes in the rolling speed.

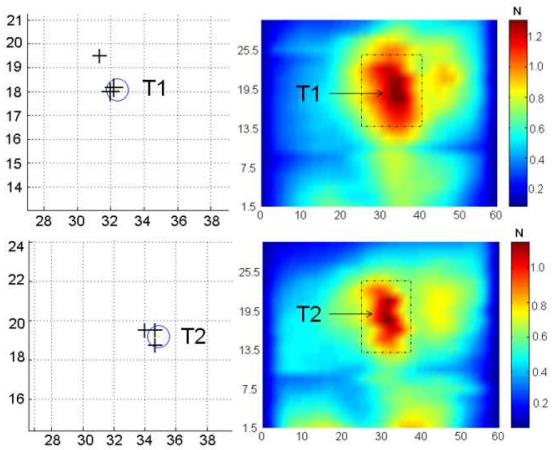

Fig. 11. The localization of T1 and T2, embedded in K_1 at a depth of 8 mm; crosshairs show the locations of the tumor, the circle indicates the registered locations of the tumors (ground truth). Left figure show a subset of the right figure to explicitly show the identified tumor locations from three tests.

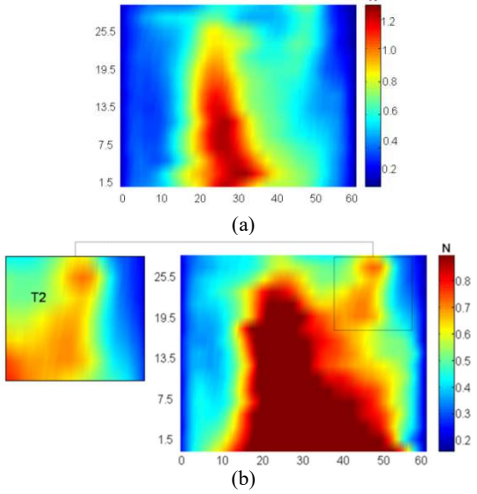

Fig.12. RMI of kidney K_2 with nodule T_2 buried at a depth of 20 mm (a) and the RMI of K_2 after apply image threshold (b); the threshold is 0.9 N, and T_2 can be explicitly identified on the Fig. 13(b); the unit of the color bars is "*N*".

3) Data Analysis: Uniaxial Palpation

To further analyze the viscoelastic properties of kidneys, uniaxial palpations were also applied to kidney sample K_1. Six locations were chosen, Fig.13. The test and analysis procedures for these tests were identical to those

carried out for the silicone phantom. The R-square errors of the fitting of $E^{(e)}(\lambda)$ are between 0.9894 and 0.9997 and the R-square errors of the fitting of $G(t)$ are between 0.9823 and 0.9943. Fig.13 (right) shows the stress-time strain functions from the chosen test regions and Table VI lists the parameters of QLV equations obtained at the different test locations. During testing, all of these stiff areas were clearly identifiable by palpating the organ by hand and we propose that providing a MIS surgeon with an intra-operatively generated RMI of a solid organ in the form of a RMI would improve the efficacy and accuracy of abnormality identification.

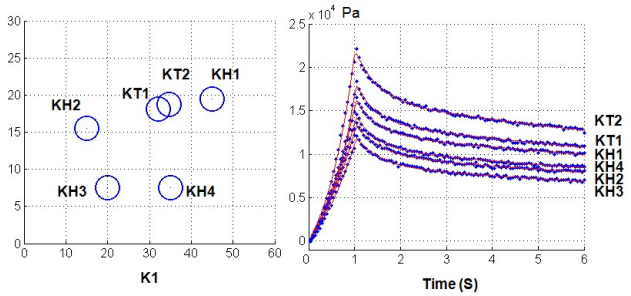

Fig.14. The locations (x, y) of the uniaxial palpation areas in kidney K_1 and the corresponding stress-time curves. The blue dots represent the experimental data, while the red solid lines represent the simulation data using the QLV model. KT1and KT2 indicates the test locations where T_1 and T_2 were embedded, respectively; KH1, KH2, KH3 and KH4 represent the locations that were nodule-free.

TABLE VI
THE PARAMETERS OF TISSUE CONSTITUTIVE EQUATION OBTAINED AT DIFFERENT TEST AREAS

	$\alpha \times 10^4$	β	C_1	C_2	V_1	V_2
KT1	0.644	14.624	0.263	0.728	2.058	0.047
KT2	0.438	15.754	0.271	0.736	2.255	0.045
KH1	0.922	9.758	0.260	0.739	2.165	0.042
KH2	0.943	8.431	0.279	0.709	1.926	0.044
KH3	0.727	9.261	0.290	0.720	1.954	0.046
KH4	0.814	9.826	0.279	0.720	2.123	0.045

IV. CONCLUSIONS AND FUTURE WORK

This paper presents a new methodology for the localization of tissue abnormalities using a force sensitive wheeled probe. By conducting a rolling wheel-tissue interaction, the stiffness distribution of an inspected area can be visualized in the form of a RMI. Following *ex vivo* tests, it is concluded that tissue abnormality localization using the technique is effective and repeatable, although a sensitivity threshold does exist. If applied in MIS, it has the potential to aid surgeons considerably in procedures that involve the accurate targeting of malignant areas, identification of precise margins for curative resection, and in improving their intra-operative diagnostic and interventional decisions. However, the constant rolling indentation depth of the current device was maintained by preregistering the soft tissue surface (i.e. creating a map of the tissue's height distribution). Preregistering a soft tissue surface is time consuming and the tissue shift during the surgery may induce inaccuracies to the surface registration. Therefore the capability of simultaneously measuring the indentation depth along the rolling path is highly desirable. As such, future work will focus on the development of a new wheeled probe which can measure the tool-tissue interaction force and the rolling indentation depth concurrently. Moreover, the presence of teeth in the wheel causes a periodic perturbation on the RMI (see Fig.6). This may potentially impair the effectiveness of the rolling indentation method, thus an in-depth examination of this effect need to be performed as part of future work.

Based on the designs proposed in [24], the envisaged prototype consists of a fibre-optic force sensor (1) attached to a spherical wheel end-effector (4) and integrates a ring-shaped pickup mechanism (3) that is connected to a fibre-optic displacement sensor (2) via a slider, as shown in Fig.14. The fibre-optic-based force sensor measures the forces acting on the wheel during rolling indentation while the ring-shaped pickup mechanism slides over the tissue surrounding the wheel. When the wheel indents into the tissue surface the pickup mechanism is free to slide axially and therefore remains on the surface of the tissue. Due to soft tissue's high local deformability, the indentation contour raises from the indentation point to the surface following an exponential curve. Therefore, by measuring the distance between the deepest indentation point and the pickup mechanism, the indentation depth can be established. The probe will be designed and manufactured to allow access through a trocar port of 14 mm or less in diameter and all components will be designed to endure standard steam sterilization. Additionally, a clinical validation of the efficacy of rolling mechanical imaging will also be carried out. A set of experiments will be conducted by surgeons and non medical individuals to investigate the pros and cons of the tissue abnormality localization approach using the wheeled indenter.

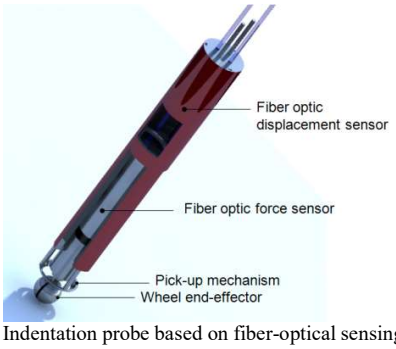

Fig.14. Rolling Indentation probe based on fiber-optical sensing scheme

REFERENCES

[1] A Cushieri, G Berci, "Laparocopic biliary surgery", Oxford: Blackwell Science, 1992.

[2] Southern Surgeons Club, "A Prospective Analysis of 1518 Laparoscopic Colecystectomies," *New England Journal of Medicine*, Vol. 324, pp 1073-1078, 1991.

[3] AM Okamura, "Methods for Haptic Feedback in Teleoperated Robot-Assisted Surgery", *Industrial Robot, An International Journal*, vol.31 (6) pp.499-508. 2004

[4] P. Puangmali, K. Althoefer, L. D. Seneviratene, D. Murphy, and P. Dasgupta, "State-of-the-art in force and tactile sensing for minimally invasive surgery", *IEEE Sensors Journal*, vol. 8, no. 4, Apr. 2008

[5] K. Xu and N. Simaan. An Investigation of the Intrinsic Force Sensing Capabilities of Continuum Robots. In *IEEE Transaction on Robotics*, Vol. 24, No. 3, pp:576-587, 2008.

[6] B Hannaford, J Trujillo, M Sinanan, et al. "Computerized endoscopic surgical grasper". In *Medicine Meets Virtual Reality*, Westwood JD,

Hoffman HM, Stredney D, et al. (eds). IOS Press: Amsterdam, The Netherlands, 265–271,1998.
[7] A Bicchi, G Canepa, D De Rossi, et al., "A sensor-based minimally invasive surgery tool for detecting tissue elastic properties", In *IEEE Int. Conf. Robot. Autom.*, Minneapolis, MN, USA; pp.884–888. 1996;
[8] G L. McCreery, A L. Trejos, MD. Naish, RV. Patel, RA. Malthaner, "Feasibility of locating tumours in lung via kinaesthetic feedback",Int. *J. Med. Robotics Comput. Assist. Surg*., vol. 4, pp.58-68, Mar. 2008.
[9] Y. Hasegawa, M. Shikida, H. Sasaki, K. Itoigawa, and K. Sato. An Active Tactile Sensor for Detecting Mechanical Characteristics of Contacted Objects. *Journal of Micromechanics and Microengineering*, 16(8):1625-632, 2006.
[10] J. Dargahi, S. Najarian, and R. Ramezanifard. Graphical Display of Tactile Sensing Data with Application in Minimally Invasive Surgery. *Canadian Journal of Electrical and Computer Engineering*, 32(3):151-155, 2007.
[11] V Egorov, S Ayrapetyan, AP Sarvazyan, "Prostate Mechanical Imaging: 3-D Image Composition and Feature Calculations", *IEEE Trans. Med. Imag.*, vol.25(10):1329-1340,2006.
[12] SP Wellman, "Tactile Imaging of Breast Masses: First Clinical Report", *Arch Surg*. 136:204-208, 2001.
[13] AP Miller, WJ Peine, JS Son, et al. "Tactile imaging system for localizing lung nodules during video-assisted thoracoscopic surgery". In *Proc. IEEE Int. Conf. Robot. Autom.*, Rome, Italy, 2996–3001. 2007.
[14] RA Beasley, RD Howe. "Tactile tracking of arteries in robotic surgery". In *Proc. IEEE Int. Conf. Robot. Autom*., Washington, DC, vol.4: 3801–3806, 2002.
[15] A.L. Trejos, J. Jayander, M.T. Perri, M.D. Naish, R.V. Patel, and R.A. Malthaner. "Robot-Assisted Tactile Sensing for Minimally Invasive Tumor Localization." The *International Journal of Robotics Research*, November 2008.
[16] A.L. Trejos, J. Jayander, M.T. Perri, M.D. Naish, R.V. Patel, and R.A. Malthaner. "Experimental evaluation of robot-assisted tactile sensing for minimally invasive surgery," *IEEE RAS/EMBS Int. Conf. Bio-med. Robot. Biomechatronics,* Scottsdale, Arizona, 2008. pp. 971–976.
[17] JD Brown, J Rosen, YS Kim, et al. "In vivo and in situ compressive properties of porcine abdominal soft tissues", *In Medicine Meets Virtual Reality II,* Westwood JD, Hoffman HM, Mogel GT, et al.(eds). IOS Press: Amsterdam, The Netherlands, pp.26–32. 2003.
[18] J Dargahi. "An integrated force–position tactile sensor for improving diagnostic and therapeutic endoscopic surgery", *Bio-Med Mater Eng,* vol.14(2): 151–166. 2004.
[19] M. Rentschler, J. Dumpert, S. Platt, K. Iagnemma, D. Oleynikov, S. Farritor, "Modeling, Analysis, and Experimental Study of In Vivo Wheeled Robotic Mobility", *IEEE Transactions on Robotics*, vol.22 (2): 308-321, 2006.
[20] AM. Okamura, C. Simone, and MD. O'Leary, "Force Modelling for Needle Insertion into Soft Tissue," *IEEE Transactions on Biomedical Engineering*, vol.51(10): 1707-1716, 2004.
[21] YC Fung. "Biomechanics: Mechanical Properties of Living Tissues". New York: Springer-Verlag, pp.269-281, 1993.
[22] D. Noonan, H. Liu, Y. Zweiri, K. Althoefer, L. D. Seneviratne, "A dual-function wheeled probe for tissue viscoelastic property identification during minimally invasive surgery", in Proc. *IEEE Int. Conf. Robot. Autom.*, Rome, Italy, pp.2629-2634. Apr. 2007.
[23] H Liu, DP Noonan, YH Zweiri, K Althoefer, LD Seneviratne, "The Development of Nonlinear Viscoelastic Model for the Application of Soft Tissue Identification", *IEEE/RSJ Int. Conf. Intelligent Robots and Systems*, pp.208-213, 2007.
[24] H. Liu, P. Puangmali, K. Althoefer, L. Seneviratne, Experimental Study of Soft Tissue Recovery Using Optical Fiber Probe, *IEEE/RSJ Int. Conf. Intelligent Robots and Systems*, San Diego, USA, pp. 516-521, 2007.

Hongbin Liu received the B.S. degree from the Northwestern Polytechnique University, Xi'an, China, in 2005 and the MSc degree from Kings College London (KCL), London, UK, in 2006 both in Mechanical Engineering.

He is currently studying for a PhD degree in KCL and a research associate in the Department of Mechanical Engineering, KCL. His research interests include intelligent grasping of robotic hand, interaction dynamics between surgical tools and soft tissue and the application of mechatronic system in medicine.

David P. Noonan received the BEng degree from Dublin City University, Dublin, Ireland, in 2005 and the MSc degree from King's College London, London, UK, in 2006, both in Mechatronic Engineering.

He is currently studying for a PhD jointly between the Institute of Biomedical Engineering and the Department of Biosurgery and Surgical Technology, Imperial College London. His current research interests include applications of mechatronics technology in medicine, articulated robotic systems and both stereo and fluorescence imaging platforms for minimally invasive surgery

Benjamin J Challacombe received his MBBS degree and the Master of Surgery from the University of London in 1998 and 2007, respectively. He was awarded the FRCS (Urol) from the Royal College of Surgeons of Edinburgh in 2008, and the Rowan Nicks Fellowship from the Royal Australasian College of Surgeons in 2009. He is currently a robotic fellow in Melbourne.

His research interests include robotic technology and telemedicine and he performed the first randomised trial of telerobotic surgery between Guy's and Johns Hopkins Hospitals in 2002. He has over 70 peer-reviewed publications and several book chapters on minimally invasive and robotic urological techniques.

Prokar Dasgupta has been an academic urologist at Guy's Hospital, London since 2002.

He is a pioneering robotic urological surgeon in the UK. He is recognized internationally for the Guy's robotic cystoprostatectomy technique. He also pioneered the minimally invasive method of delivering Botulinum toxin to refractory overactive bladders named the Dasgupta technique. He has over 250 publications including over 100 peer-reviewed papers. He has received 25 awards including the prestigious Jack Lapides Prize, Geoffrey Chisholm Gold Medal and the 2006 Karl Storz-Harold Hopkins Golden Telescope.

Lakmal D. Seneviratne (M'03) obtained his B.Sc. (Eng.) and Ph.D. degree in mechanical engineering from King's College London (KCL) where he currently is a professor in mechatronics at KCL.

His research interests include robotics and intelligent autonomous systems. He has published over 175 refereed research papers related to mechatronics. He is a Fellow of both the IET and the IMechE**.**

Kaspar Althoefer (M'02) holds a degree in electronic engineering from the University of Technology Aachen, Germany. He received Ph.D. degree from the Department of Electrical and Electronic Engineering at King's College London (KCL) in 1997. He is now a Reader in the Department of Mechanical Engineering at KCL.

He has being engaged in research on mechatronics since 1992 and gained considerable expertise in the areas of sensing, sensor signal analysis, embedded intelligence and sensor data interpretation using neural networks and fuzzy logic as well as robot-based applications. He has co-authored over 120 peer-reviewed research papers related to mechatronics.